Acoustic Characterization and Prediction of Representative, Small-Scale Rotary-Wing Unmanned Aircraft System Components

Nikolas S. Zawodny *Research Aerospace Engineer*
D. Douglas Boyd Jr. *Senior Research Engineer*
Casey L. Burley *Senior Research Engineer*
Aeroacoustics Branch, NASA Langley Research Center
Hampton, VA 23681-2199

ABSTRACT

In this study, hover performance and acoustic measurements are taken on two different isolated rotors representative of small-scale, rotary-wing unmanned aircraft systems (UAS) for a range of rotation rates. Each rotor system consists of two fixed-pitch blades powered by a brushless motor. For nearly the same thrust condition, significant differences in overall sound pressure level (OASPL), up to 8 dB, and directivity were observed between the two rotor systems. Differences are shown to be in part attributed to different rotor tip speeds, along with increased broadband and motor noise levels. In addition to acoustic measurements, aeroacoustic predictions were implemented in order to better understand the noise content of the rotor systems. Numerical aerodynamic predictions were computed using the unsteady Reynolds-averaged Navier Stokes code OVERFLOW2 on one of the isolated rotors, while analytical predictions were computed using the Propeller Analysis System of the Aircraft NOise Prediction Program (ANOPP-PAS) on the two rotor configurations. Preliminary semi-empirical frequency domain broadband noise predictions were also carried out based on airfoil self-noise theory in a rotational reference frame. The prediction techniques further supported trends identified in the experimental data analysis. The brushless motors were observed to be important noise contributors and warrant further investigation. It is believed that UAS acoustic prediction capabilities must consider both rotor and motor components as part of a combined noise-generating system.

NOTATION

C_T	Rotor thrust coefficient
c	Rotor blade element chord, m
Δf	Narrowband frequency resolution, Hz
H	Blade element trailing edge bluntness, m
M_{tip}	Rotor tip Mach number
N_c	Number of coils in brushless motor
N_p	Number of poles/magnets in brushless motor
N_{revs}	Number of rotor revolutions
R	Rotor tip radius, m
Re_c	Reynolds number based on chord
Δr	Blade element width, m
T	Rotor thrust, N (lbs.)
α_0	Blade element zero-lift angle of attack, deg.
β	Blade element geometric pitch, deg.
ε_r	Normalized autospectral random uncertainty, %
θ	Observer elevation angle, deg.
λ_∞	Imposed rotor inflow ratio, $U_\infty/\Omega R$
$\sigma_{p_{rms}}$	Standard deviation of pressure, Pa
ψ	Blade element trailing edge solid angle, deg.
Ω	Rotor rotation rate, RPM (rad/s)

INTRODUCTION

The past several years have witnessed a considerable increase in the presence of and market for unmanned aircraft systems (UAS) in the United States National Airspace System (NAS). One of the major challenges facing the Federal Aviation Administration (FAA) is the requirement to institute appropriate policies of regulation to address this increased vehicle demand. Since May of 2014, private companies have been able to file petitions for exemption from obtaining certificates of waiver or authorization (COAs) to permit non-recreational UAS operations for a set of controlled, low-risk situations (Refs. 1, 2). Of the first 500 commercial UAS exemptions granted by the FAA, 71% are rotary-wing in nature (Ref. 3). Of these rotary-wing vehicles, more than 90% are of the multi-copter variety.

According to the FAA (Ref. 2), UAS are categorized as "small" if they have an overall weight of less than 55 pounds. The increase in the number of multi-copter small-scale UAS (sUAS) in the NAS warrants an understanding of the possible impacts that these vehicles will have on the civilian population. One of these impacts is how they are acoustically perceived by humans. The ability to predict the noise generated by these vehicles is important to aiding in the selection and/or design of future vehicle configurations that are deemed suitable for specified missions. It is currently unknown how well current conventional rotorcraft noise prediction methods will apply to sUAS; however, previous studies

indicate noise-scaling issues for vertical lift vehicles characterized by low Reynolds numbers (Ref. 4). The goal of this work is to acoustically characterize two off-the-shelf sUAS rotor systems of similar performance through measurement and prediction analyses. The rotor blades investigated in this study are for vehicles that weigh less than 10 pounds, which are in the lower range of sUAS as defined by the FAA.

This paper begins with an overview of the theoretical noise source mechanisms associated with rotary-wing vehicles. This is followed by a description of the experiments performed and the noise prediction methods implemented. Experimental performance and acoustic results for two different rotor blade configurations will be compared against one another as well against their predicted counterparts.

BACKGROUND

Noise Source Mechanisms

The most common and identifiable rotor noise sources attributable to rotary-wing vehicles shown pictorially in Figure 1 can be broadly divided into deterministic and non-deterministic components. The deterministic components include the following (Ref. 5):

- **Thickness noise**: noise due to displacement of fluid by the rotor blade,
- **Loading noise**: noise due to force exerted on the fluid by the rotor blade surface,
- **Blade vortex interaction noise**: impulsive loading noise due to a tip vortex impacting a following blade, and
- **High-speed impulsive noise**: high-intensity, in-plane noise associated with high advancing tip speeds (transonic flow).

Non-deterministic loading noise - also known as broadband noise - is the result of turbulent flow interactions on or near the blade surface. The sources of broadband rotor noise include

- **Turbulence ingestion noise** (Ref. 6): unsteady loading noise due to ingestion of atmospheric turbulence into the rotor,
- **Blade wake interaction noise** (Ref. 7): noise caused by blade interactions with rotor wake turbulence, and
- **Blade self noise** (Refs. 8, 9): noise produced by scattering of turbulent flow over the blade trailing edge.

To date, attention has primarily been focused on prediction of the deterministic components of rotor aerodynamic noise. This is because full-scale helicopters have high rotor tip speeds, which result in high acoustic amplitudes at the rotor blade passage frequency (BPF) and its associated harmonics. These tonal amplitudes have conventionally dwarfed the contribution of broadband noise to the overall acoustic signature. However, prior research has shown broadband helicopter noise to be an important overall contributor for certain flight conditions and directionalities (Refs. 7, 9).

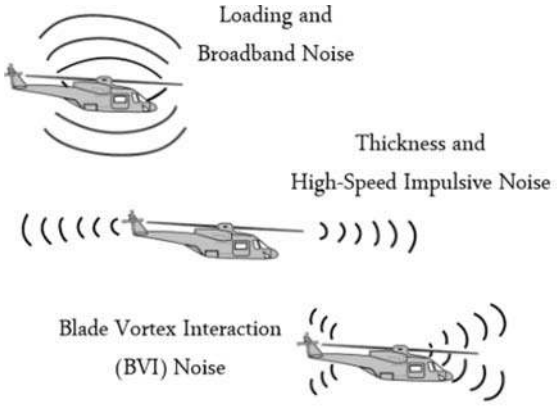

Fig. 1. Primary rotor aerodynamic noise sources and associated directionalities for modern-day, full-scale helicopters (Adapted from Ref. 5).

The Unknowns of sUAS Noise

Small-scale UAS (sUAS) provide an interesting challenge to the tasks of noise characterization and prediction. While the fundamental aerodynamically-generated source mechanisms remain consistent with those associated with full-scale helicopters, there are numerous unknowns warranting investigation. These include the effects of the reduced size of the vehicles compared to conventional rotorcraft, the effects of multiple rotors, the balance between tonal and broadband noise, the relative contributions of rotor blade aerodynamic noise and motor noise, and the appropriate noise metrics with which to categorize the vehicles.

An important attribute of the considerably smaller sizes of rotary-wing sUAS as compared to conventional rotorcraft is the different flow speed regime that they encounter. This flow regime is commonly defined in terms of two important non-dimensional parameters: the tip Mach number and chord-based Reynolds number at 75% span. These are respectively defined as

$$M_{\text{tip}} = \frac{\Omega * R}{a_\infty}, \qquad Re_c(0.75R) = \frac{\rho_\infty * \Omega * 0.75R * c}{\mu_\infty}, \qquad (1)$$

where Ω is the rotor rotation rate, R is the rotor tip radius, a_∞ is the ambient speed of sound, ρ_∞ is the ambient air density, c is the rotor blade chord (in this case at the 75% span location), and μ_∞ is the ambient air dynamic viscosity. It is not uncommon for full-scale helicopters to exhibit an advancing tip Mach number in the range of $0.7 \leq M_{\text{tip}} \leq 0.8$, whereas a sUAS multicopter would exhibit one in the range of $0.15 \leq M_{\text{tip}} \leq 0.3$. Furthermore, a representative Reynolds number based on the chord at $0.75R$ of a full-scale helicopter is typically on the order of $Re_c(0.75R) \sim 10^6$, while that for a sUAS multicopter is $Re_c(0.75R) \sim 10^4 - 10^5$. In terms of conventional flat plate aerodynamics, the former of these Reynolds number ranges would fall well into the turbulent flow regime, while the latter would fall into the laminar-transitional flow regime. This lack of dynamic similarity results in questions

regarding application of conventional rotorcraft noise prediction tools to platforms of such combined low tip Mach numbers and representative Reynolds numbers (Ref. 4).

As was stated previously, analysis and prediction of noise generated by rotary-wing vehicles has been primarily focused on the deterministic components of noise. However, with the reduced scale of sUAS, the relative importance of tonal and broadband noise contributions is unknown. The reduced tip speeds of these vehicles are such that high-speed impulsive noise is an unlikely contributor, whereas the laminar-transitional flow speeds to which the vehicle blades are subjected can have considerable broadband self-noise contributions (Ref. 8). For a case in which a rotary-wing UAS exhibits acoustic tones related to the BPF that are comparable in amplitude to higher frequency broadband noise, the latter mechanism may become one of concern for characterization and modeling.

TECHNICAL APPROACH

Experimental Setup

Illustrations of the experimental setup utilized in this study are provided in Figure 2. Experiments were performed in the Structural Acoustic Loads and Transmission (SALT) anechoic chamber facility at the NASA Langley Research Center (Ref. 10). This facility is acoustically treated down to a cut-off frequency of 100 Hz and has interior dimensions (wedge tip to wedge tip) of 4.57-m (15-ft) high, 7.65-m (25-ft) wide, and 9.63-m (31.6-ft) long. A total of five 1/4" Type 4939 free-field Brüel & Kjaer microphones in an arc array configuration are positioned in the acoustic far-field of the rotor test stand in elevation angle increments of 22.5°, from 45° below the plane of the rotor to 45° above the plane of the rotor. Specifically, the microphones are positioned at a radial distance of 1.905 m (75 in.) from the motor hub. This distance corresponds to at least 13R for the rotors tested in this study. The rotor test stand itself was constructed so that the plane of the rotor would stand 2.29-m (7.5-ft) above the floor wedge tips, which corresponds to half of the room height.

The physical rotation rate of the motor outer casing was measured using a laser sensor-tachometer. The tachometer provided both a DC voltage as well as a Transistor-Transistor Logic (TTL) pulse signal indicating each revolution of the motor housing. Both of these signal outputs served as a measure of the rotation rate of the rotor-motor apparatus. In addition, a single-axis Honeywell Type 31 load cell is positioned directly underneath the motor for measuring thrust (see Figure 2(c)). This close proximity of the load cell to the rotor assisted with reducing loading uncertainties associated with longer moment arms and wake loading. Thrust measurements are non-dimensionalized in the form of the thrust coefficient, which is defined as

$$C_T = \frac{T}{\rho_\infty \pi R^2 (\Omega R)^2}. \tag{2}$$

All data were acquired at a sampling rate of 80 kHz for a duration of 30 seconds.

(a) SALT Facility

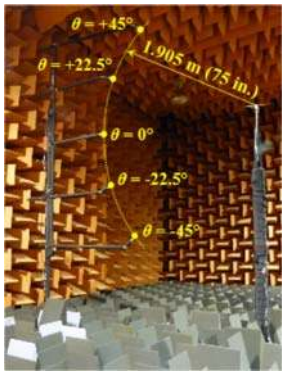

(b) Microphone Array

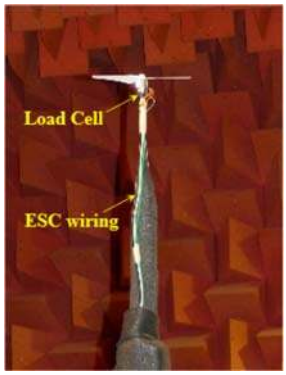

(c) Rotor-Motor Apparatus

Fig. 2. Experimental apparatus within the SALT facility.

Two rotors were selected for analysis in this study based on research of common UAS platforms and component availability. The first rotor is a carbon fiber replica of one sold by DJI, a multi-copter UAS manufacturer. The model of the original rotor from the manufacturer is the DJI 9443 (the rotor is herein referred to as the DJI-CF rotor). The second rotor is an injection-molded slow flyer propeller manufactured by Advanced Precision Composites[r] . The model of this rotor from the manufacturer is the APC 11X4.7SF, which is herein referred to as the APC-SF rotor. An image of these rotors, as well as their respective radial chord and blade pitch angle distributions, is provided in Figure 3, while their physical parameters are provided in Table 1. The chord and pitch angle data of the DJI-CF rotor shown in Figure 3(b) were extracted from a high-resolution laser scan of the blade surfaces, while those for the APC-SF were retrieved from the UIUC propeller database of Ref. 11. As a result of having a fine resolution computational surface grid of the DJI-CF rotor, accurate radial section profiles were able to be extracted for input into the blade element aero-analysis, which is discussed in the next section. As for the APC-SF rotor, the radial blade section profiles are a blending from an Eppler63-type airfoil near the hub to a Clark-Y-type airfoil near the tip (as indicated by the manufacturer). Actual profiles of this rotor were not available for this study. Therefore, the software CROTOR (Ref. 12) was used to create a blended blade profile interpolation between these two airfoil shapes along the span of the blade.

The rotors were driven by the same electronic speed controller (ESC) but different motors, as indicated in Table 1. While this does present a potential inconsistency between the two rotors regarding motor acoustic content, this is believed to be minimal due to the fact that they are of nearly identical size and have the same number of coils and magnetic poles within the motor housings. Specifically, both motors have $N_c = 12$ coils and $N_p = 14$ magnetic poles.

(a) Rotor Planforms

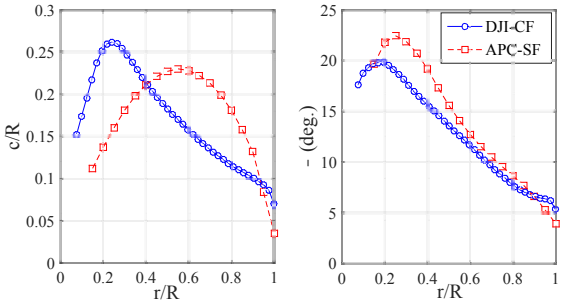

(b) Rotor Chord and Pitch Distributions

Fig. 3. Images and geometric data of rotors analyzed in this study. Note: APC-SF geometry data obtained from Ref. 11.

Table 1. UAS rotor parameters.

Parameter	Rotor 1	Rotor 2
Name	DJI-CF	APC-SF
Diameter,[a] in. (m)	9.4 (0.24)	11.0 (0.28)
Weight, g (oz.)	12.1 (0.43)	15.0 (0.53)
Motor, Manuf. (Model)	DJI (2212)	3DR (2830-358)
ESC, Manuf. (Model)	DJI (OPTO E300)	

[a]As quoted by manufacturers.

It is important to note that only hover conditions were investigated in this study. Because the SALT facility is a sealed room, operation of the rotors for a long time results in recirculation build-up, which can compromise the desired static condition. Evidence of recirculation was found when the voltage output of the load cell began to exhibit high-amplitude fluctuations indicative of turbulent gust ingestion into the rotor disk area. Therefore, acoustic data used for post-processing were limited to a time period preceding this apparent onset of recirculation. To maintain consistency across the different rotors and RPM conditions, a time period of five seconds was established for acoustic data post-processing across all test conditions. The upper and lower limit testing conditions for each rotor are defined in terms of both RPM and Reynolds number based on chord at 75% tip radius ($Re_c(0.75R)$) in Table 2. Experimental data points were taken between these condition limits in increments of 300 RPM.

Table 2. UAS rotor testing condition limits.

Rotor		Lower Limit	Upper Limit
DJI-CF			
	RPM	3000	7200
	$Re_c(0.75R)$	3.0×10^4	6.8×10^4
APC-SF			
	RPM	1800	5100
	$Re_c(0.75R)$	3.8×10^4	1.1×10^5

Noise Prediction Methodology

The overall noise prediction process is outlined by the flowchart presented in Figure 4. Noise predictions are divided into deterministic (or tonal) noise and random (or broadband) noise, both of which require knowledge of the aerodynamic conditions experienced by the rotor blades. The blade aerodynamics are computed using either computational fluid dynamics (CFD), or blade element analysis. Once the blade aerodynamics are computed, the deterministic components of noise are computed using an impermeable Ffowcs Williams and Hawkings solver. Broadband noise is computed semi-analytically using the Broadband Acoustic Rotor Codes (BARC) software suite (Ref. 9). This software suite predicts rotor self-noise from models developed by Brooks et al. (Ref. 8) for isolated airfoils, and later extended to a model for rotating blades (Ref. 9). The experimental database that forms the basis for this method is believed to be applicable to the current study due to comparable Reynolds and Mach numbers between it and the rotor blades under current investigation.

CFD Simulations

CFD simulations were performed on the DJI-CF rotor geometry using OVERFLOW2 (Ref. 13), which is an unsteady Reynolds-averaged Navier-Stokes (URANS) code. This code was chosen based on previous successes with predicting rotor blade loadings and acoustics for a scaled model of a helicopter main rotor (Ref. 14). The simulation is time-marching in nature, in which multiple rotor revolutions are performed until convergence is obtained. The optimized second order backward differencing formulation BDF2OPT was utilized with a fixed number of 50 Newtonian sub-iterations per physical time-step. As a result of this fixed number of sub-iterations, the $L_\infty-$norm(RHS) orders of convergence at each sub-iteration varied between 3 and 5 depending on the simulation case. Spatial differencing was performed using a fourth order central differencing for inviscid terms and a second order central differencing for viscous terms. The Spalart

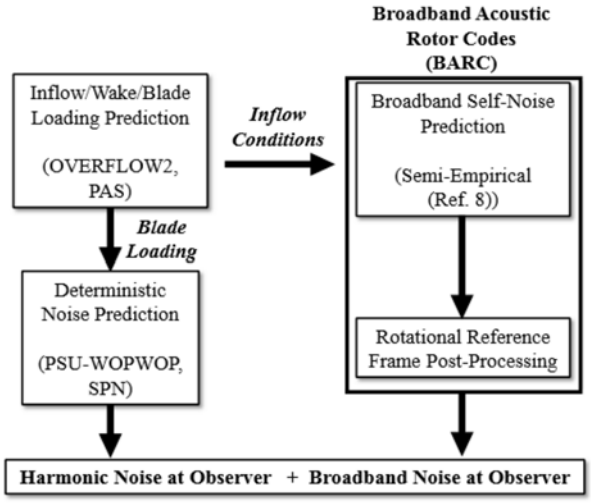

Fig. 4. Flowchart of the current noise prediction method.

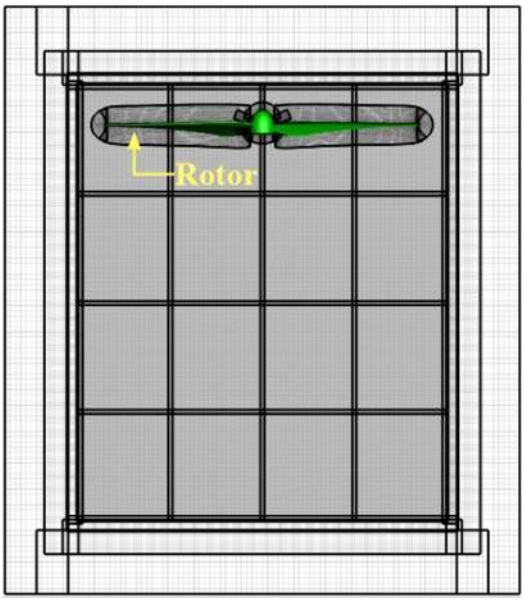

Fig. 5. Cross-section view of the first five grid levels of OVERFLOW2 computational domain.

and Allmaras with rotation/curvature correction (SARC) one-equation turbulence model along with a Detached Eddy Simulation (DES) was utilized. The computational grid was constructed using overset grid generation via the Chimera Grid Tools v2.1 software package (Ref. 15). The volume grid is divided into a total of thirteen levels, the first of which contain the near-body grids immediately surrounding the rotor blades and hub. The remaining twelve levels are Cartesian off-body grids, the first level of which has a uniform spacing of approximately 2.5% of the mean blade chord. The finest Cartesian grid extends to 1.175R horizontally from the hub center and to 0.25R above and 2.5R below the rotor disk plane. The boundaries of the computational domain extend out to 125R. The near-body and first level off-body grids make up approximately 95.5% of the total 260 million grid points that define the computational domain. One full revolution took approximately 30 hours to simulate using 1,008 computer cores on the NAS Pleiades supercomputer, with convergence in thrust and torque being typically obtained by the fifth revolution of the rotor. An illustration of the core CFD computational domain is provided in Figure 5.

Acoustic predictions are performed using the CFD-provided impermeable loading data on the blade surfaces. These data are input into the PSU-WOPWOP code (Ref. 5), a FW-H solver, to compute acoustic pressure time histories at defined observer locations. One single rotor revolution's worth of CFD data is computed at a physical time resolution corresponding to 0.25° azimuthal increments, and input into the acoustic solver in 1° azimuthal increments and run as a periodic case. As a result, this computational procedure is considered to provide a measure of the deterministic (or tonal) components of noise. The process in which the impermeable blade surface loadings from OVERFLOW2 are used to compute an acoustic prediction using PSU-WOPWOP is herein denoted as OF2-PSW.

Blade Element Analysis

A more computationally efficient prediction method that is more amenable to use in the vehicle design process was also studied. The method implemented in this study is ANOPP-PAS (Ref. 16), which is herein referred to as PAS. While PAS is originally intended for analysis of propellers in a fixed-wing configuration, it is selected for consideration in this study due to its complete set of capabilities. The blade profile analysis modules of PAS include a coordinate transformation using a Joukowski transformation, potential flow around the blades computed by Theodorsen's method using the Kutta condition to fix circulation, and boundary layer analysis using the Holstein-Bohlen or Truckenbrodt methods for respective laminar and turbulent regions. Propeller performance and induced flow are then computed using Lock's method with the Prandtl circulation function for the blade tip region. Finally, a Subsonic Propeller Noise (SPN) module (see Figure 4) is utilized for computing acoustic pressure time histories and spectra at defined observer locations. This noise module is a direct implementation of Farassat's F1A FW-H acoustic solver (Refs. 17, 18). The PAS computation time encompassing all the mentioned modules for a rotor blade discretized into 35 sections takes approximately one minute on a high-performance laptop computer. This computation time is in stark contrast to the previously-mentioned required CFD simulation time using OVERFLOW2 of more than six days for five full rotor revolutions.

Because PAS was developed for modeling propellers in flight, a freestream velocity condition is used for non-dimensionalization purposes. To use PAS in the current application, a small non-zero freestream velocity was specified,

which is equivalent to imposing a uniform inflow condition. The freestream velocity was iteratively adjusted until the predicted rotor thrust was within 5% of the experimental measurement. It is worth noting that the imposed rotor inflow ratio reached an upper limit value of $\lambda_{\infty,\max} = 0.03$ across all tested conditions. This does have the effect of reducing the effective angle of attack experienced by the individual blade elements, and thus the loading of the blade. The effects of this will be investigated in the following Results section.

Self-Noise Prediction

As shown in Figure 4, blade self-noise prediction is computed based on inflow conditions along the blade computed either using OVERFLOW2 or PAS. The BARC suite implements a blade element analysis technique in which the noise contributions of the individual blade elements are summed to yield the total blade noise. It is formulated based on the noise-boundary layer correlation data of Ref. 8, which are for NACA 0012 airfoil sections. The modeled noise source mechanisms are well-documented in Refs. 8,9 and are summarized as follows:

- **Turbulent Boundary Layer-Trailing Edge (TBL-TE) Noise**: noise due to pressure scattering from convection of turbulence of the trailing edge,
- **Turbulent Boundary Layer-Separation/Stall (TBL-SS) Noise**: TBL-TE noise at high angles of attack due to convection of larger-scale turbulent structures past the trailing edge,
- **Laminary Boundary Layer-Vortex Shedding (LBL-VS) Noise**: noise due to vortex shedding past the trailing edge coupled with aerodynamic feedback loops associated with laminar boundary layer development,
- **Trailing Edge Bluntness-Vortex Shedding (TEB-VS) Noise**: vortex shedding noise from a blunt trailing edge, and
- **Tip Vortex Formation (TVF) Noise**: noise due to formation and shedding of the blade tip vortex.

Of the source mechanisms listed above, the LBL-VS is not included in the predictions in this study. This is because it is believed that three-dimensional flow over the surface of the rotor blades disrupts the occurrence of the chord-wise feedback mechanism required for LBL-VS to occur. All broadband noise predictions performed in this study utilize the boundary layer curve data of Ref. 8 corresponding to an untripped blade section.

The inflow conditions computed using either OVERFLOW2 or PAS serve as inputs to BARC. In addition to local blade element flow conditions (angle of attack, resultant flow velocity), geometric parameters of the local blade elements are also needed. These include blade geometric pitch angle (β), blade chord length, trailing edge bluntness (H), trailing edge solid angle (ψ), width of the blade segment (Δr), and the zero-lift angle of attack of the blade element (α_0). This last quantity is very important, as it serves as the reference for determining the "effective" local angle of attack on which the boundary layer curves of Ref. 8 are based. A test for determining α_0 was conducted by performing a 2-dimensional steady OVERFLOW2 simulation on the blade profile of the DJI-CF rotor at the 75% span location over a range of geometric angles of attack. Lift and drag conditions were recorded from which a zero-lift angle could be determined. The Improved Blade Aerodynamics (IBA) module of PAS (Ref. 16) was then used to compute the same quantity on the same blade profile. The resulting zero-lift angle computed in IBA was found to be within 0.2° of that computed using OVERFLOW2. Therefore, it was decided that the IBA module of PAS be used to determine the α_0 values for all blade element profiles analyzed in this study.

Noise Metrics

Three acoustic metrics are used in this study for comparisons between predictions and experiment. They are the sound pressure level (SPL) spectrum, the overall sound pressure level (OASPL), and the A-weighted OASPL (Ref. 19).

RESULTS

The results of this study are divided into five sections. The first section discusses the performance of the rotors in terms of static thrust and power draw, with comparisons between computational and experimental data. The second section briefly discusses post-processing techniques implemented on the experimental acoustic data. The third section presents experimental acoustic data of both rotors for a range of rotor rotation rates. The final two sections discuss tonal predictions at principal rotor-associated frequencies with experimental comparisons and some preliminary broadband acoustic prediction results.

Rotor Performance

Figure 6(a) shows the measured C_T variation with RPM for the two rotors. Note that measurement uncertainties are indicated in the form of error bars, which were computed using the conventional root-sum-squares (RSS) method. The uncertainty variables accounted for are the 95% confidence intervals of the raw acquired load data, the bias uncertainty of the load cell, and the 95% confidence intervals of the acquired RPM data. As the experimental data show, the total computed uncertainties in thrust coefficient decrease with increasing RPM. This is because the largest contributing component to the uncertainty is the load cell bias uncertainty. Included in this figure are static thrust coefficient data for the APC-SF rotor provided by Ref. 11, and the predicted thrust coefficients from the OVERFLOW2 simulations of the DJI-CF rotor at three different RPMs. Comparison of the current thrust measurements of the APC-SF rotor with the published reference data show reasonable agreement, with curve fit deviations of

less than 2% between the two data sets. Furthermore, comparison between the OVERFLOW2 predictions and the measured DJI-CF thrust data also show agreement to within 2.5%. It is important to note that thrust predictions using PAS are not shown in this figure due to the iterative process utilized based on a desired thrust condition.

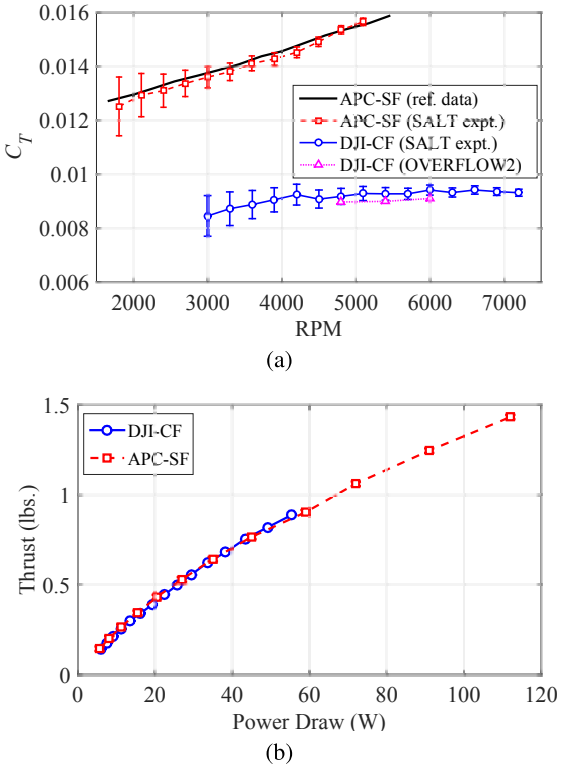

Fig. 6. Rotor thrust performance comparisons: (a) thrust coefficient vs. RPM with APC-SF reference data (Ref. 11), (b) dimensional thrust vs. power draw.

Figure 6(b) shows the trends of dimensional thrust as a function of power draw for the two rotor-motor configurations. The purpose of this plot is to demonstrate that while the two rotors are intended to operate over different RPM ranges (as indicated in Figure 6(a)), they exhibit very similar thrust generation profiles. This means that the APC-SF rotor can be used to generate the same amount of thrust as the DJI-CF rotor at a lower RPM with a comparable amount of power draw. This has important implications because blade-generated noise generally decreases with decreasing tip Mach number.

Acoustic Measurement Post-Processing

The acquired acoustic data are processed three ways. The first and simplest method is to simply treat the acquired time data as a random data set. Acoustic narrowband spectra were computed using the fast Fourier Transform (FFT) with a Hanning window of 75% overlap and a frequency resolution of 5 Hz. As stated previously, only five seconds of acquired acoustic data were utilized for post-processing for a given RPM condition. This was both because of the onset of recirculation as well as RPM drift for longer motor run times. As a result of this, the autospectral random uncertainty was fairly large at $\varepsilon_r = 14.14\%$ (Ref. 20). This translates to a random SPL uncertainty of $u_{r,SPL} \in \{-0.66, +0.57\}$ dB.

The second post-processing technique utilized on the acoustic data emulates a deterministic analysis. The purpose of this method is to more accurately compare acoustic amplitudes at principal frequencies of interest - namely harmonics of the BPF - between predictions and experiment. For the current study, analysis was limited to the first two harmonics of the BPF. To isolate the acoustic contributions at these specific frequencies, a 3rd-order Butterworth narrow bandpass filter was applied to the time series data, with a $\pm$ 40 Hz frequency band centered around the frequency of interest. The TTL pulse signal from the tachometer was used to parse the time series data into blocks corresponding to individual revolutions of the rotor. Acoustic amplitudes of each frequency of interest were computed by calculating the RMS of the ensemble-averaged pressure time history across all revolutions:

$$SPL_{n*BPF} = 20\log_{10}\left[\frac{\bar{p}_{rms}}{p_{ref}}\right]. \quad (3)$$

Furthermore, the uncertainties of these tonal amplitudes were approximated by the 95% confidence intervals of the RMS pressure values:

$$u_{SPL_{n*BPF}} = 20\log_{10}\left[\frac{\bar{p}_{rms} \pm 1.96\sigma_{p_{rms}}/\sqrt{N_{revs}}}{p_{ref}}\right]. \quad (4)$$

These uncertainties were typically within the bounds of the autospectral random uncertainty defined previously.

The third post-processing technique implemented on the experimental acoustic data is similar to the previous one, however with the goal of extracting the non-periodic, or broadband noise in the microphone signals. This was done again by parsing the time series data into blocks of rotor revolutions, then computing a mean rotor revolution time history. This mean revolution time history was then subtracted from the individual time blocks, which are then FFT-processed as a random time series. The primary drawback of these latter two techniques is that they do not account for fluctuations in the rotor rotation rate. In other words, all time blocks were defined to be the same length, which enforces a condition of constant RPM. As a result of this, these techniques would yield higher uncertainties in the ensemble-averaged pressure values at higher frequencies due to phase drift and retain higher frequency tonal content in the broadband-extracted spectrum for a run condition in which the RPM was seen to vary by a considerable amount.

Experimental Spectra and OASPL Directivities

Figures 7(a) and 7(b) show acoustic spectra of the APC-SF and DJI-CF rotors at respective rotation rates of $\Omega = 4200$

RPM (70 Hz) and 5400 RPM (90 Hz), at an observation angle of $\theta = -45°$ (below the rotor plane). These figures clearly illustrate a high-amplitude tone at the respective BPFs of 140 and 180 Hz, as well as additional tonal content at the 2nd-4th BPF harmonics. There is also a discernible tone at 1.5*BPF for the DJI-CF rotor, which is believed to be due to differences in blade-to-blade geometry. Also provided in these figures are the acoustic spectra of the isolated unloaded motors used for each of these rotors at the same rotation rates. It can be seen that the isolated motors contribute a considerable amount of tonal spectral content over a frequency range corresponding to approximately 10-14 shaft harmonics. The motor used with the APC-SF rotor is also seen to contain broadband acoustic energy in the frequency range of 500 Hz to 1 kHz. Observation of the rotor-motor spectra for both cases show that the tone of highest amplitude that is apparently due to the motors corresponds to a frequency of $N_p * \Omega$, which is related to the mechanical "cogging" torque generated as a result of the rotation of the motor outer casing (Ref. 21). There are numerous other tones in the motor-only spectrum that are believed to contribute to the rotor-motor spectrum; however, they cannot be quantified because the effects of rotor blade loading on the motor noise were not investigated in this study.

Plots of the spectral content of both rotors including motor noise for a range of rotation rates are provided in Figures 8 and 9. Both rotors show an increase in BPF acoustic amplitude with increasing rotation rate. The APC-SF rotor spectra in Figure 8 also show an increase in the 2*BPF harmonic with increasing rotation rate, which correspond to dimensional frequencies of 240, 280, and 320 Hz. The DJI-CF rotor spectra of Figure 9, however, do not show a distinct increasing trend in 2*BPF acoustic levels. It is also interesting to observe appreciable broadband acoustic energy for both rotors for frequencies at and above 1 kHz. The APC-SF rotor shows a spectral floor of nearly constant energy between 1 and 10 kHz (except for the lowest shown rotation rate of 3600 RPM), while the DJI-CF rotor shows a spectral floor of increasing acoustic amplitude up to approximately 20 kHz. An interesting observation is how the high frequency broadband levels of the DJI-CF rotor are slightly lower for the 6000 RPM case as compared to those of the two lower rotation rates. The exact cause of this is unknown; however, deflections of the rotor blades at high rotation speeds may be a possibility. The location of high-frequency spectral roll-off appears to increase with increasing RPM for both rotors.

Illustrations of the broadband spectrum extraction technique applied to the APC-SF and DJI-CF rotors are provided in Figures 10 and 11, respectively. The broadband extraction results show effective removal of the lower frequency BPF harmonics for both rotor cases. The 1/3-octave results also show a gradual increase in mid- and high-frequency broadband spectral content with decreasing angle of observation. This is in agreement with the notion that unsteady loading noise increases with radiation angles away from the plane of the rotor. Only the negative observation angle results are shown since similar behaviors are observed for their positive angle counterparts. The APC-SF rotor results show a considerable amount of retained higher frequency tonal content that is believed to be in part due to motor noise. The DJI-CF results, however, show much cleaner broadband spectra with much less retained mid- and high-frequency tonal content. This is because the DJI-CF rotor was observed to exhibit rotation rate fluctuations on the order of ± 3 RPM for the case shown. The APC-SF rotor, on the other hand, was observed to exhibit rotation rate fluctuations on the order of ± 20 RPM for the case shown. This is also believed to be the cause for the lower broadband-extracted levels relative to the floor of the raw spectra over a frequency range of 5-12 kHz in Figure 10. These results demonstrate the challenges associated with extracting the broadband levels for the case of a rotor-motor configuration exhibiting considerable RPM variations. However, the current results are still useful for extracting broadband acoustic trends.

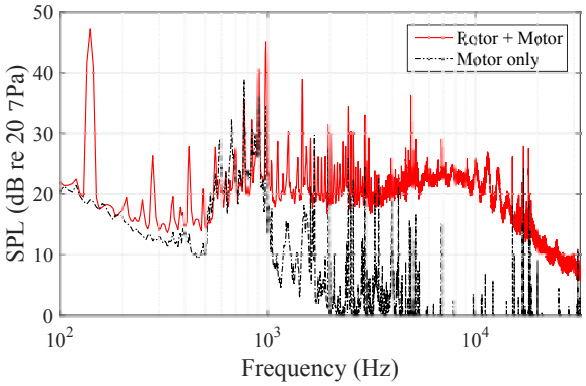

(a) APC-SF rotor, $\Omega = 4200$ RPM

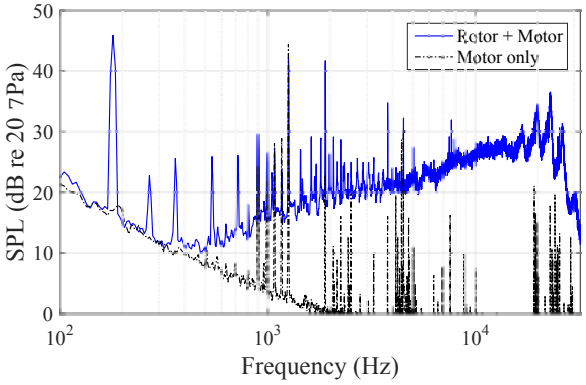

(b) DJI-CF rotor, $\Omega = 5400$ RPM

Fig. 7. Acoustic narrowband spectral comparison of APC-SF and DJI-CF rotor-motor and motor-only configurations. ($\theta = -45°$)

The partial directivities of unweighted and A-weighted OASPL for both rotors are shown in Figure 12. Note that both OASPL metrics are calculated over a frequency range of 100Hz $\leq f \leq$ 20 kHz. Figure 12(a) shows an overall increase in OASPL for the APC-SF rotor at all measured observer angles with increasing rotor rotation rate. This is not the case for the DJI-CF rotor results of Figure 12(b), which show very

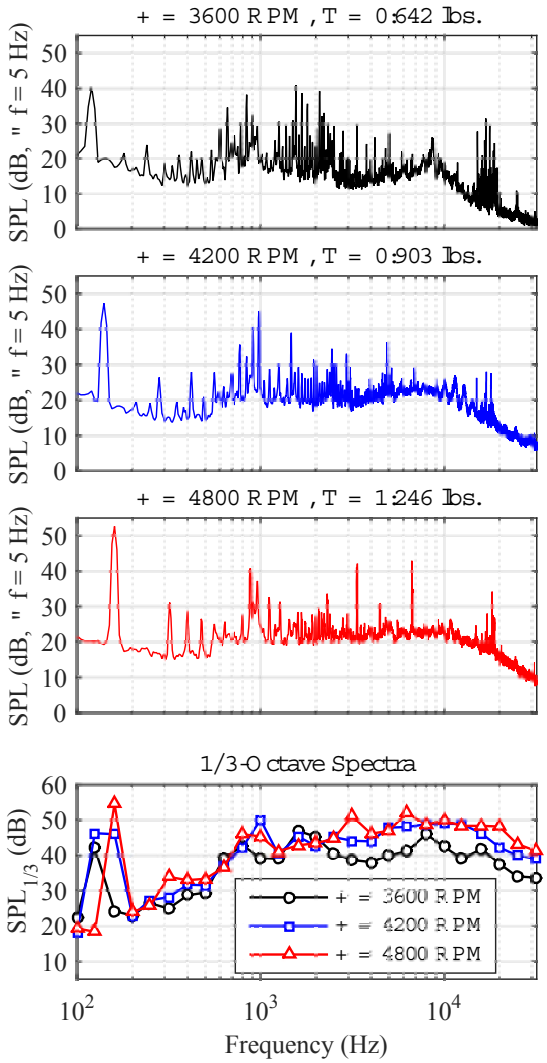

Fig. 8. Acoustic spectra for the APC-SF rotor at different rotation rates ($\theta = -45°$).

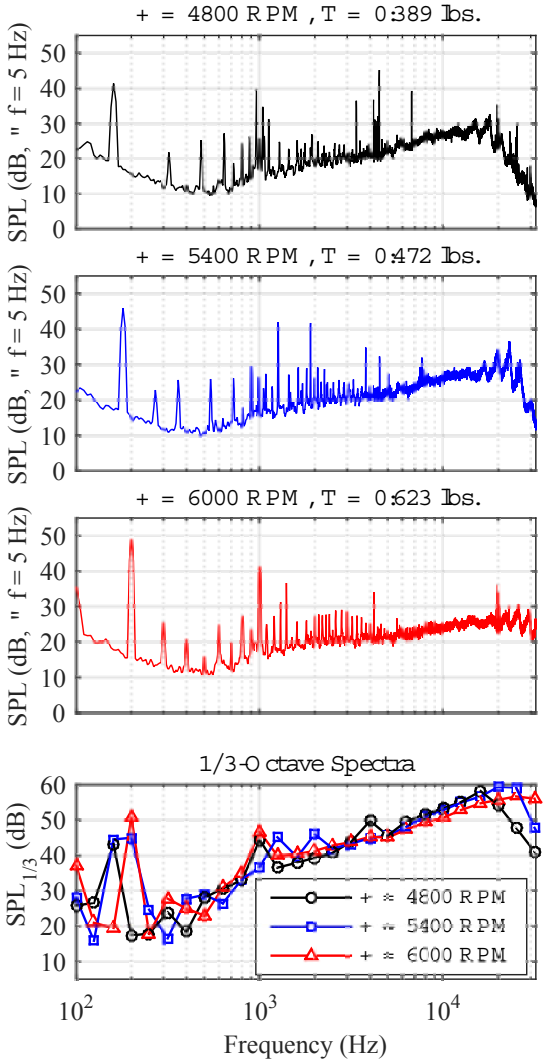

Fig. 9. Acoustic spectra for the DJI-CF rotor at different rotation rates ($\theta = -45°$).

similar unweighted OASPLs and a surprising decrease in A-weighted OASPLs with increasing rotor rotation rate. Despite the previously mentioned increase in the BPF acoustic amplitudes with increasing rotor rotation rates, the presence of higher-frequency broadband noise and loaded motor noise make it difficult to extract simple acoustic trends based on rotor rotation rate. This implies that better physical understanding and modeling of both brushless motor noise and rotor blade self-noise are needed to more accurately characterize such sUAS component configurations. The acoustic predictions performed in the remainder of this paper focus on the deterministic aerodynamically-generated noise from the rotor blades and some preliminary investigation into characterizing broadband noise source mechanisms of the rotor blades. Brushless motor noise characterization is left for future work.

The thrust performance data of Figure 6 showed that both rotors produce similar thrust over different rotation rates. The APC-SF rotor is intended to operate over considerably lower rotation rates as compared to the DJI-CF rotor. Therefore, due to the potential noise benefit of a rotor operating at a lower tip speed, it is useful to compare the OASPL directivities between the two rotors for a common thrust condition. Examples of such occur at $\Omega = 6000$ RPM for the DJI-CF rotor and $\Omega = 3600$ RPM for the APC-SF rotor. These run conditions yielded rotor thrust levels of $T = 0.623$ lbs. (2.77 N) and $T = 0.642$ lbs. (2.86 N), respectively. Figure 13 shows the unweighted and A-weighted OASPL partial directivity patterns for the two rotors under these run conditions. Overall, the APC-SF rotor is observed to offer a noise reduction benefit as compared to the DJI-CF rotor, particularly for out-of-plane observer angles. Specifically, the APC-SF rotor offers an unweighted OASPL benefit up to 8 dB at $\theta = +45°$, and 6.5 dB at $\theta = -45°$. The noise benefits at negative observation an-

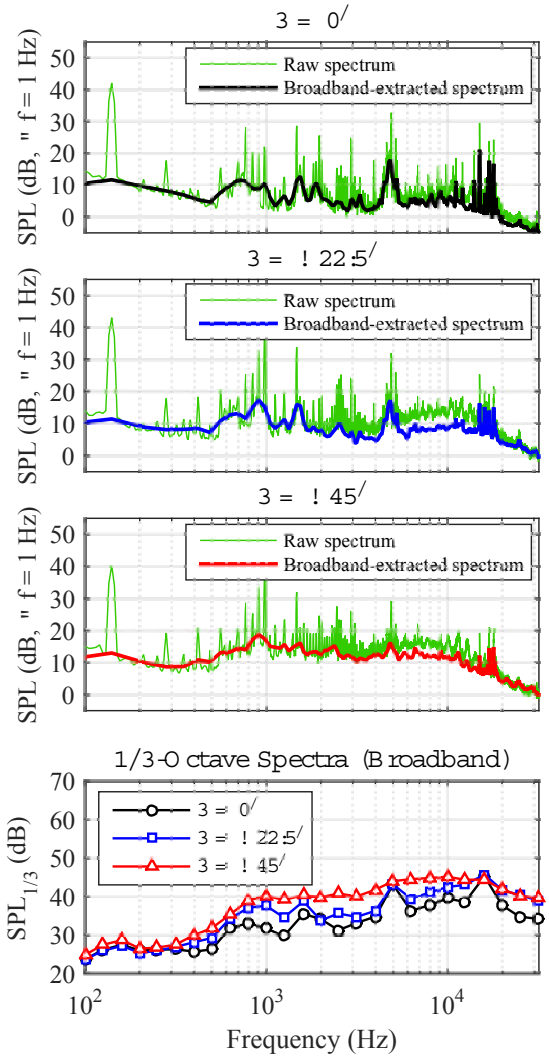

Fig. 10. Broadband spectra extraction results for the APC-SF rotor ($\Omega = 4200$ RPM).

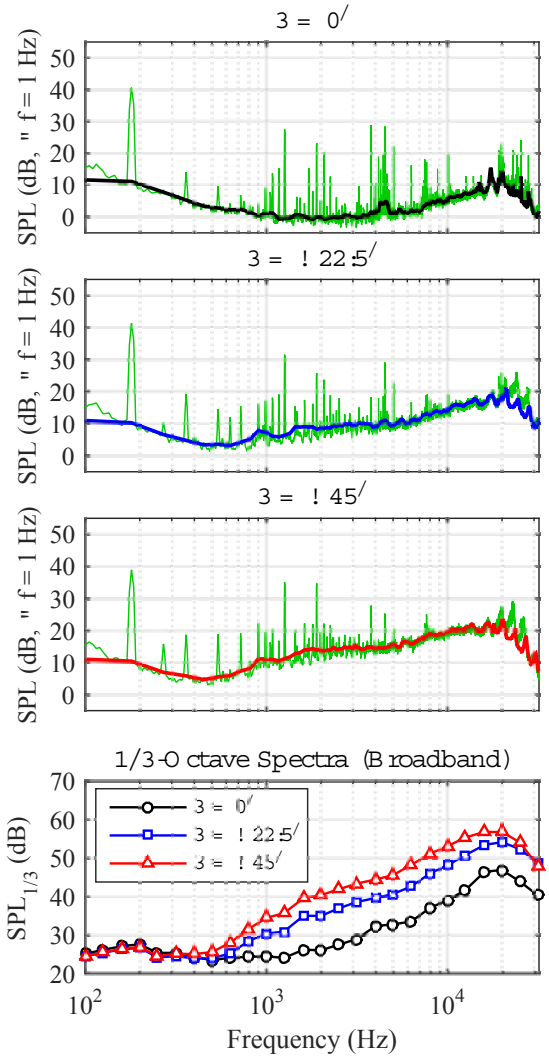

Fig. 11. Broadband spectra extraction results for the DJI-CF rotor ($\Omega = 5400$ RPM).

gles are considered to be more important since they represent locations indicative of vehicle flyover conditions. These benefits are seen to be reduced, however, with the application of A-weighting to the spectra. This is believed to be primarily due to the additional noise of the motor in the mid-frequency range, over which the A-weighting is highest. A-weighting is also seen to yield an OASPL value for the APC-SF rotor at the in-plane observer location of $\theta = 0°$ that is higher than that for the DJI-CF rotor at the same location. Again, this is believed to be heavily influenced by loaded motor noise. Despite the reduced noise benefits implied with the presence of noise from different motors and A-weighting, there are still observed noise benefits of 1.8 and 3.6 dBA at respective observer angles of $\theta = -22.5°$ and $\theta = -45°$. This still represents a considerable noise reduction for observer locations that are representative of vehicle flyover conditions.

Tonal Noise Predictions

The deterministic components of noise are predicted using either the OF2-PSW or PAS methods. OF2-PSW was only carried out on the DJI-CF rotor because this was the only rotor for which a high-resolution computational surface grid was available. A summary of the simulated conditions presented for the duration of this paper are provided in Table 3. These RPMs were selected based on the manufacturer-quoted nominal operation ranges of these rotors.

Table 3. Rotor simulation runs.

Rotor	RPMs	Sim. method
DJI-CF	4800, 5400, 6000	OF2-PSW, PAS
APC-SF	3600, 4200, 4800	PAS

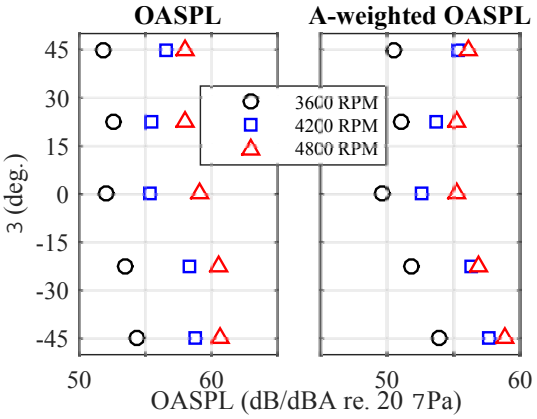

(a) APC-SF rotor

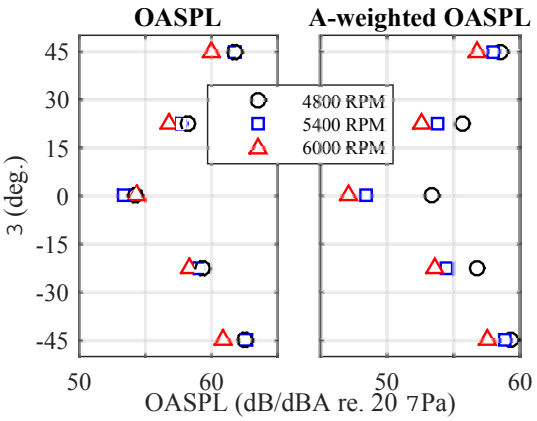

(b) DJI-CF rotor

Fig. 12. Unweighted and A-weighted OASPL partial directivities for APC-SF and DJI-CF rotor-motor configurations.

An acoustic comparison between the two prediction techniques and experimental data for the DJI-CF rotor are shown in Figure 14. Figures 14(a) and14(b) show the BPF and 2*BPF directivities computed from the two simulation techniques across the elevation angle range of $-90^\circ \leq \theta \leq 90^\circ$, divided into their thickness, loading, and total noise components. The rightmost plots in these figures also have the experimental values included for comparison, which were computed using the ensemble-averaging technique mentioned previously. The BPF directivity predictions show excellent agreement with each other and the experimental data, particularly in terms of matching the directivity shape trends. The maximum discrepancy between prediction and experiment in Figure 14(a) is less than 2.5 dB. The 2*BPF harmonic, however, shows considerable discrepancies in loading and total noise directivity behavior between the two predictions. OF2-PSW predicts a trough in the total noise directivity at this frequency, which is due to the thickness and loading noise being out of phase with and of comparable amplitude to one another. PAS, however, does not predict this behavior.

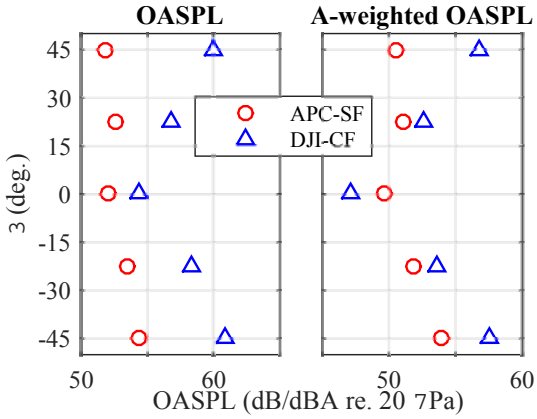

Fig. 13. Unweighted and A-weighted OASPL partial directivities for APC-SF and DJI-CF rotor-motor configurations for common thrust conditions. (DJI-CF rotor, $\Omega = 6000$ RPM; APC-SF rotor, $\Omega = 3600$ RPM)

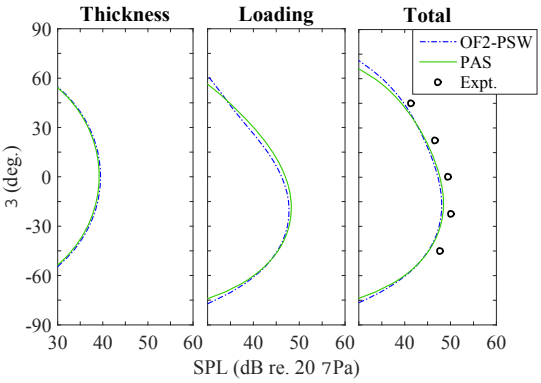

(a) BPF (180 Hz) Directivity

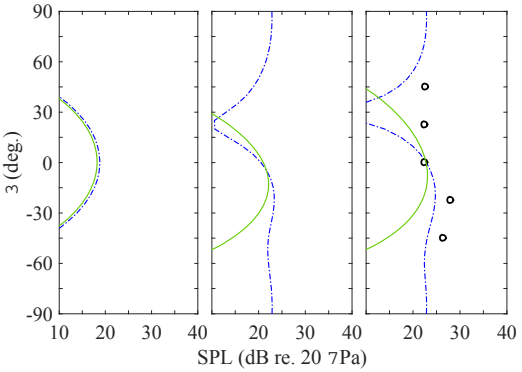

(b) 2*BPF (360 Hz) Directivity

Fig. 14. Tonal acoustic directivity predictions with comparison to experiment of DJI-CF rotor at $\Omega = 5400$ RPM.

The abilities of the two prediction techniques to capture directivity characteristics are investigated further for the 2*BPF harmonic across the three simulated rotation rates in Figure 15. The predictions in this figure represent the total noise at the 2*BPF harmonic consisting of the summation of thickness and loading noise contributions. The OF2-PSW results show an interesting directivity trend with increasing RPM, in which the location of the previously mentioned trough due to phase cancellation of thickness and loading noise sources shifts to higher angles with increasing RPM. An increase in RPM also increases the prominence of the loading noise, which results in better agreement between the OF2-PSW and PAS predictions over a wider range of propagation angles. The experimental data appear to agree better with the OF2-PSW predictions at 4800 and 5400 RPM, while both predictions are comparable to the available experimental data at 6000 RPM. The discrepancies between PAS and OF2-PSW predictions at the 2*BPF harmonic are hypothesized to be related to three-dimensional flow effects along the blade span which are not modeled in PAS. While the 2*BPF harmonic contains acoustic energy that is well below that of the BPF for the majority of observation angles, different flight conditions may increase the importance of this and higher frequency BPF harmonics. For the current hover cases investigated, however, the BPF is the frequency of primary concern.

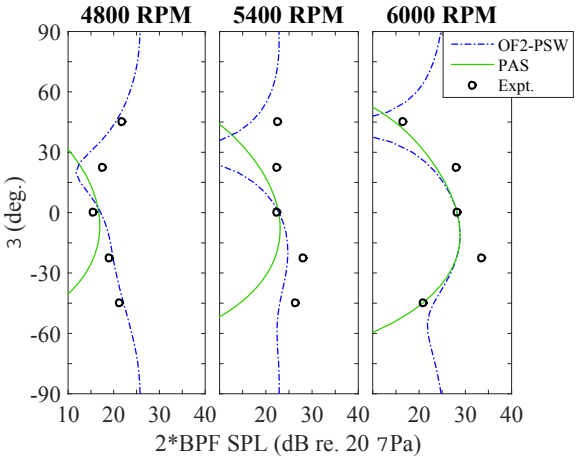

Fig. 15. Total noise directivity predictions of 2*BPF harmonic for DJI-CF rotor with comparison to experimental data.

PAS was run on both rotors for the conditions indicated in Table 3, the resulting BPF acoustic amplitudes of which are shown in Figure 16(a). These results show excellent overall agreement in terms of directivity trends and levels, with a maximum discrepancy of less than 2.5 dB across all shown conditions. Therefore, for the case of such small rotors in a clean hover condition, PAS appears to be a suitable, computationally efficient alternative over computationally expensive CFD. The BPF predictions of the two rotors for the case of similar thrust generation are also shown in Figure 16(b). The results show the DJI-CF rotor to have higher BPF acoustic levels than the APC-SF due to higher tip speed. Based solely on the experimental data, the APC-SF rotor offers a noise benefit increasing from 3.6 dB at $\theta = +45°$ to 8.9 dB at $\theta = -45°$. In addition to this reduction in acoustic levels, the reduction in BPF between these two conditions (120 Hz versus 200 Hz) offers a potential human perception benefit based on a metric such as A-weighting of SPL.

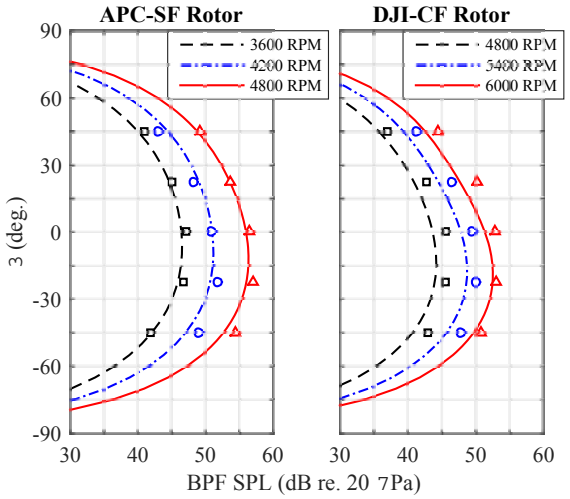

(a) PAS Predictions for Different RPM

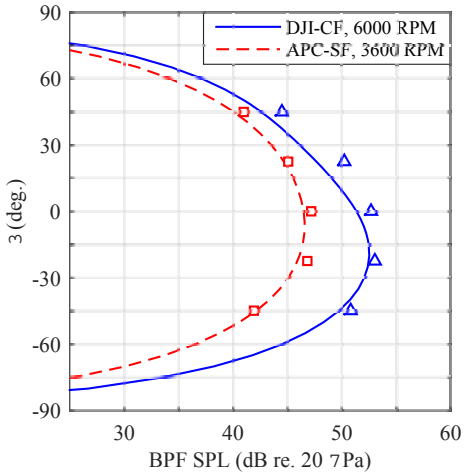

(b) PAS Predictions for Similar Thrust Conditions

Fig. 16. Total noise predictions at BPF using PAS for the two rotors. (Note: lines represent predictions, symbols represent experiments)

Preliminary Broadband Noise Predictions

The BARC analysis code is used to predict broadband noise in the form of 1/3-octave spectra. BARC requires the local inflow conditions at each blade section, which were computed using either OVERFLOW2 or PAS in this study. Since CFD

simulations were not able to be performed on the APC-SF rotor in this study, preliminary broadband predictions are performed for both rotors using the PAS-generated inflow data. It is important to note that the following predictions are considered preliminary for two primary reasons. First, the current requirement of a non-zero freestream velocity by PAS makes it a questionable source for reliable inflow data extraction. Second, application of BARC assumes that the boundary layer curves corresponding to NACA 0012 airfoils are applicable to the rotors currently being investigated. This is not necessarily an appropriate assumption since the blade profiles of the current rotors deviate considerably from NACA 0012 airfoils, both in terms of thickness and camber distribution. Nonetheless, at this stage, BARC is valuable for identifying the pertinent broadband noise source mechanisms and scaling trends.

The individual source mechanisms that contribute to the total broadband noise are presented for both rotors in Figure 17 for the rotation rates corresponding to comparable thrust generation. The corresponding experimental spectra after implementing the broadband-extraction technique discussed previously are also provided. As these results show, the TBL source mechanisms are predicted to be prominent broadband noise sources for both rotors. Note that the combined contributions of the turbulent boundary layer noise sources are presented as $\text{TBL}_{\text{Total}}$ in Figure 17, which represents the summation of the TBL-TE_{p}, TBL-TE_{s}, and TBL-SS source mechanisms. Low frequency broadband noise is predicted to be strictly due to boundary layer separation effects (TBL-SS). This is attributed to the higher angles of attack experienced by both rotors along the inboard portions of their blades, promoting flow separation at or near the trailing edge. Furthermore, this source mechanism, along with suction-side turbulent boundary layer noise (TBL-TE_{s}), dominates for higher frequency noise on the APC-SF rotor. As for the DJI-CF rotor, broadband noise at high frequencies is seen to transition from TBL-TE noise to trailing-edge bluntness (TEB-VS) noise. This makes sense because the trailing edges of the DJI-CF rotor blades were measured to be considerably thicker with very small trailing edge solid angles as compared to the APC-SF rotor. Specifically, the mean trailing edge thickness of the DJI-CF rotor was measured to be 40 times larger than that for the simulated APC-SF blade profiles. Figure 17(a) also shows considerable broadband under-prediction for the majority of the shown frequency range as compared to the experimental data. However, the presence of a prominent peak at the 1/3-octave band center frequency of 1 kHz illustrates a frequency region where the broadband extraction technique was not effective. Therefore, a refinement of this broadband extraction technique is planned for future work.

The performance of the broadband noise prediction is gauged by testing its behavior for different flow conditions. The broadband prediction results for three different rotation rates are shown in Figure 18 for the APC-SF rotor. The overall trends of the broadband predictions with respect to rotation rate are seen to agree with the experimental data. However,

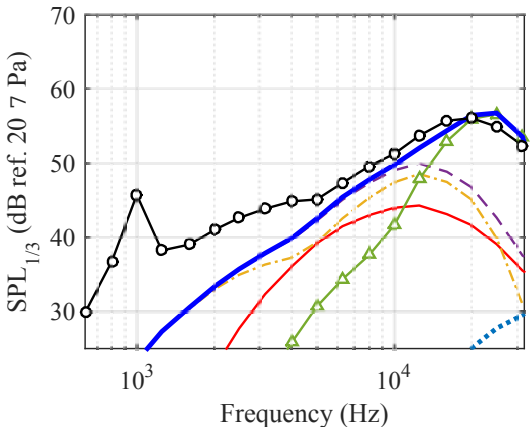

(a) DJI-CF rotor, $\Omega = 6000$ RPM

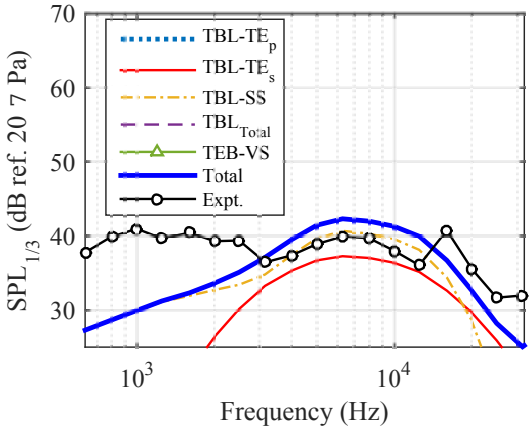

(b) APC-SF rotor, $\Omega = 3600$ RPM

Fig. 17. Component noise source breakdown for broadband predictions for the two rotors. ($\theta = -45^\circ$)

there is seen to be under-prediction across the mid-frequency range of 630 Hz $\leq f \leq$ 3.15 kHz for all rotation rates and over-prediction at mid- to high-frequencies (3.15 kHz $\leq f \leq$ 12.5 kHz) for $\Omega = 3600$ RPM, which is shown in greater detail in Figure 17(b). It is worth noting that observation of the experimental narrowband spectra of the broadband-extracted signals for these cases (see Figure 10) revealed a considerable amount of retained mid-frequency tonal content and lower broadband levels at high frequencies due to appreciable fluctuations in the rotation rates of the rotor. This is believed to be a contributor to the broadband noise under-prediction at the middle frequencies and the over-prediction at higher frequencies.

CONCLUSIONS AND FUTURE WORK

This study presents thrust and acoustic data for two rotor configurations representative of rotary-wing sUAS under static hover conditions at different rotor rotation rates. Tonal noise associated with the rotor BPF and associated harmonics was identified, along with a considerable amount of mid- and high-frequency broadband noise. In addition, the brushless motors used in this study were also experimentally shown to have

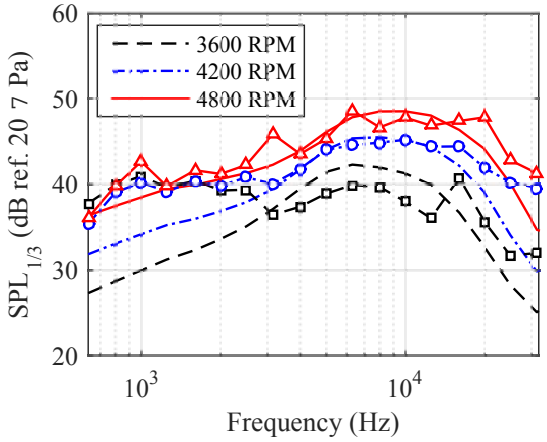

Fig. 18. Broadband predictions at different rotor rotation rates for the APC-SF rotor with comparison to experimental data at $\theta = -45^{\circ}$. (Note: lines represent predictions, symbols represent experiments)

prominent tonal noise contributions over a frequency range of high human sensitivity. The APC-SF rotor was able to achieve a comparable amount of thrust generation to the DJI-CF rotor, but at lower rotor rotation rate and, thus, at lower tip speeds. This rotor system was found to offer considerable noise reduction benefits. Unweighted and A-weighted OASPL noise reduction benefits were quantified at 6.5 dB and 3.6 dBA, respectively, at an observer angle representative of vehicle flyover conditions. Further analysis of this observed behavior is planned with the goals of identifying principal blade geometry features that can lead to quieter small-scale rotor configurations.

Tonal acoustic predictions were performed utilizing both high-fidelity CFD (OVERFLOW2) and blade element analysis (PAS), while preliminary broadband acoustic predictions were performed using a semi-empirical method (BARC). The tonal acoustic prediction results using both techniques match the experimental data well at the rotor BPF, which is the frequency of dominant tonal acoustic energy for the static hover cases analyzed. These results indicate that a computationally efficient prediction method such as PAS may be suitable for acoustic characterization of sUAS rotors in static hover conditions. Preliminary broadband noise predictions using the BARC identified broadband source mechanisms and scaling trends across different rotor geometries and rotor rotation rates. Further investigations into trailing edge boundary layer behavior for representative UAS blade profiles at appropriate flight Mach and Reynolds numbers are planned. Additional efforts are also underway to investigate forward flight effects on the resulting radiated noise, both experimentally and computationally.

The results of this study indicate that both the rotors and motors of rotary-wing sUAS require consideration for accurately assessing acoustic impacts of these vehicles on human populations. Further investigations into the effects of blade loading on the motor noise are planned in efforts to develop low-fidelity motor noise models.

Author contact

Nikolas S. Zawodny, nikolas.s.zawodny@nasa.gov

ACKNOWLEDGMENTS

The authors would like to acknowledge Mr. Jaye Moen of the Aeroacoustics Branch and Mr. Matthew Hayes of the Structural Acoustics Branch at NASA Langley Research Center for their assistance with experimental setup and testing. The authors would also like to acknowledge Dr. Douglas Nark of the NASA Langley Structural Acoustics Branch for his assistance with rotor modeling using ANOPP-PAS. This work was funded by NASA's Convergent Aeronautical Systems (CAS) sub-project, the Design Environment for Novel Vertical Lift Vehicles (DELIVER), the principal investigator of which is Dr. Colin Theodore.

REFERENCES

[1]112th Congress, *Subtitle B – Unmanned Aircraft Systems*, Public Law 112-95, 2012.

[2]FAA, *Fact Sheet – Unmanned Aircraft Systems (UAS)*, Available at: http://www.faa.gov/news/fact_sheets/news_story.cfm?newsId=18297, 2015.

[3]Kesselman, S., *Snapshot of the First 500 Commercial UAS Exemptions*, Association for Unmanned Vehicle Systems International (AUVSI), 2015.

[4]Shenoy, R. K., Kohlhepp, F. W., and Leighton, K. P., *Acoustic characteristics of 1/20-scale model helicopter rotors*, Sikorsky Aircraft Division, Stratford, CT, NASA CR 177355, 1986.

[5]Brentner, K. and Farassat, F., "Modeling aerodynamically generated sound of helicopter rotors," *Progress in Aerospace Sciences*, Vol. 39, Apr 2003, pp. 83–120.
doi: 10.1016/S0376-0421(02)00068-4

[6]Amiet, R. K., *Noise Produced by Turbulent Flow Into a Rotor: Theory Manual for Noise Calculation*, East Hartford, CT, NASA CR 181788, 1989.

[7]Brooks, T. F. and Burley, C. L., "Blade Wake Interaction Noise for a Main Rotor," *Journal of the American Helicopter Society*, Vol. 49, (1), 2004, pp. 11–27.
doi: 10.4050/JAHS.49.11

[8]Brooks, T., Pope, D. S., and Marcolini, M. A., *Airfoil Self-Noise and Prediction*, Hampton, VA, NASA RP 1218, 1989.

[9]Burley, C. L. and Brooks, T. F., "Rotor Broadband Noise Prediction with Comparison to Model Data," *Journal of the American Helicopter Society*, Vol. 49, (1), 2004, pp. 28–42.
doi: 10.4050/JAHS.49.28

[10]Grosveld, F. W., "Calibration of the Structural Acoustics Loads and Transmission Facility at NASA Langley Research Center," InterNoise 99, 1999.

[11]Brandt, J. B., Deters, R. W., Ananda, G. K., and Selig, M. S., *UIUC Propeller Database*, Department of Aerospace Engineering, University of Illinois at Urbana-Champaign, Retrieved from http://m-selig.ae.illinois.edu/props/propDB.html.

[12]Carter, P., *CROTOR extensions to XROTOR*, Esotec Developments, Retrieved from http://www.esotec.org/sw/crotor.html.

[13]Nichols, R. H. and Buning, P. G., *User's Manual for OVERFLOW 2.2*, NASA Langley Research Center, Available at http://overflow.larc.nasa.gov/home/users-manual-for-overflow-2-2/.

[14]Boyd, D. D., "HART-II Acoustic Predictions using a Coupled CFD / CSD Method," American Helicopter Society 65th Annual Forum, 2009.

[15]Chan, W. M., Gomez III, R. J., Rogers, S. E., and Buning, P. G., "Best Practices in Overset Grid Generation," 32nd AIAA Fluid Dynamics Conference, 2002.

[16]Nguyen, L. C. and Kelly, J. J., *A Users Guide for the NASA ANOPP Propeller Analysis System*, Hampton, VA, NASA CR 4768, 1997.

[17]Farassat, F., "Linear Acoustic Formulas for Calculation of Rotating Blade Noise," *AIAA Journal*, Vol. 19, (9), Sep 1981, pp. 1122–1130.
doi: 10.2514/3.60051

[18]Farassat, F., *Derivation of Formulations 1 and 1A of Farassat*, Hampton, VA, NASA TM 2007-214853, 2007.

[19]Bennett, R. L. and Pearsons, K. S., *Handbook of Aircraft Noise Metrics*, Canoga Park, CA, NASA CR 3406, 1981.

[20]Bendat, J. S. and Piersol, A. G., *Random Data Analysis and Measurement Procedures*, John Wiley & Sons Inc., third edition, 2000, Chapter 6: Statistical Errors in Advanced Estimates, pp. 316–348.

[21]Ko, H.-S. and Kim, K.-J., "Characterization of Noise and Vibration Sources in Interior Permanent-Magnet Brushless DC Motors," *IEEE Transactions on Magnetics*, Vol. 40, (6), Nov 2004, pp. 3482–3489.
doi: 10.1109/TMAG.2004.832991